

Generation of induced alveolar assembloids with functional alveolar-like macrophages

Received: 3 July 2023

Accepted: 22 March 2025

Published online: 09 April 2025

 Check for updates

Ji Su Kang^{1,2,7}, Youngsun Lee^{3,7}, Youngsun Lee^{1,2,7}, Dayeon Gil^{3,7}, Min Jung Kim^{1,3}, Connor Wood⁴, Vincent Delorme⁴, Jeong Mi Lee^{1,2}, Kyong-Cheol Ko¹, Jung-Hyun Kim^{1,3,5,6}✉ & Mi-Ok Lee^{1,2}✉

Within the human lung, interactions between alveolar epithelial cells and resident macrophages shape lung development and function in both health and disease. To study these processes, we develop a co-culture system combining human pluripotent stem cell-derived alveolar epithelial organoids and induced macrophages to create a functional environment, termed induced alveolar assembloids. Using single-cell RNA sequencing and functional analyses, we identify alveolar type 2-like cells producing GM-CSF, which supports macrophage tissue adaptation, and macrophage-like cells that secrete interleukin-1 β and interleukin-6, express surfactant metabolism genes, and demonstrate core immune functions. In response to alveolar epithelial injury, macrophage-like cells efficiently eliminate damaged cells and absorb oxidized lipids. Exposure to bacterial components or infection with *Mycobacterium tuberculosis* reveals that these assembloids replicate key aspects of human respiratory defense. These findings highlight the potential of induced alveolar assembloids as a platform to investigate human lung development, immunity, and disease.

The human lung is a complex organ vital for breathing and maintaining physiological homeostasis. These processes are executed by the alveolar epithelium, which forms a physical barrier that protects the lung from potentially harmful inhaled agents, and alveolar macrophages (AMs), an abundant immune cell population which takes up residence on the luminal surface of alveoli after birth^{1,2}. Alveolar epithelial cells (AECs), comprising alveolar type I (AT1) and type II (AT2) cells, facilitate gas exchange and produce surfactant to prevent alveolar collapse^{3,4} whereas AMs phagocytose inhaled particles, pathogens, and apoptotic cells, thereby contributing to the clearance of potentially harmful substances from the respiratory system. AMs also maintain optimal lung function by clearing excess or aged surfactant⁵. The coordinated interactions between AECs and

macrophages are instrumental for both lung development and adult lung function, and when these go awry, contribute to the progression of respiratory diseases^{2,6,7}. Such disease-initiating mechanisms remain largely unknown due to the lung's complexity and the lack of suitable research models. Although experiments conducted on primary human cells have provided important insights, such approaches face challenges in terms of scalability, reproducibility, and mimicking the complex cellular microenvironment^{8,9}.

Organoid technology has been pivotal for enabling studies of disease-associated cellular phenotypes and mechanisms in human-relevant contexts, and has also been instrumental for studying AEC biology^{10,11}. However, in the lung, as in other organs, the presence of immune cells such as macrophages is an important component of

¹Korea Research Institute of Bioscience and Biotechnology (KRIBB), Daejeon 34141, Republic of Korea. ²KRIBB School of Bioscience, University of Science and Technology (UST), Daejeon 34113, Republic of Korea. ³Division of Intractable Diseases Research, Department of Chronic Diseases Convergence Research, Korea National Institute of Health, Cheongju, South Korea. ⁴Tuberculosis Research Laboratory, Discovery Biology, Institute Pasteur Korea, Seongnam 13488, Republic of Korea. ⁵College of Pharmacy, Ajou University, Suwon 16499, Korea. ⁶Research Institute of Pharmaceutical Science and Technology, Ajou University, Suwon 16499, Republic of Korea. ⁷These authors contributed equally: Ji Su Kang, Youngsun Lee, Youngsun Lee, Dayeon Gil.

✉ e-mail: doctorkim@ajou.ac.kr; molee@kribb.re.kr

tissue function in both health and disease, and thus far, studies of alveolar epithelial organoids (iAEOs) have not incorporated immune cells, significantly limiting insights gained about their physiological functions⁹. Separately, recent advances in cellular reprogramming and differentiation techniques have enabled the generation of induced macrophages (iMφ) from human pluripotent stem cells (hPSCs). These iMφ possess the basic properties of primary human macrophages, making them a highly valuable resource for studying macrophage biology and macrophage-related diseases^{12,13}. While several research groups have recently made efforts to integrate macrophages into lung organoids or lung slices^{14,15}, there remains a significant gap in understanding how to optimize culture conditions to preserve the function and properties of iAEO and iMφ. Overcoming these limitations would represent a pivotal step towards investigating the functionality and adaptability of iMφ within a tissue-like context.

Herein, we set out to combine iMφ and iAEOs in an in vitro platform we named 'iAlvAssemb' to assess their properties and interactions. By developing a specialized medium that supported co-culture of iAEOs and iMφ, while preserving their distinct functional characteristics, we were able to comprehensively characterize their cellular properties, evaluate interactive responses, and explore cell-type specific roles in tissue homeostasis and disease, including lung injury and infection.

Results

Generation of iAlvAssemb by co-culturing iAEO and iMφ

To develop iAlvAssemb containing functional macrophages, we first generated iAEOs and iMφ from identical hPSC lines as previously reported^{10,12,13}. For the differentiation of iAEO, step-wise differentiation was performed and differentiation efficiency was validated flow cytometer analysis (Supplementary Fig. 1a, b). The iAEOs were characterized by staining with Lysotracker (Fig. 1a), immunostaining of iAEC-specific markers, including NKX2.1, SFTPC, Muc1, and HOPX (Fig. 1b, c and Supplementary Fig. 1c), and Transmission Electron Microscopy (TEM) imaging to confirm lamellar bodies formation (Fig. 1d). Similarly, we validated that the iMφ expressed macrophage-specific cell surface markers, including CD45, CD14, and CD11c (Fig. 1e, f and Supplementary Fig. 1d), and activated transcription of macrophage-related genes such as *PTPRC*, *CD14*, and *IL1B* (Fig. 1g).

We then set out to define a cell culture medium that would support identity of each cell type. When we evaluated whether iAEOs maintained viability and proliferative capacity when cultured in iMφ media, we found that iAEOs did not survive (Supplementary Fig. 2a), and conversely, when we cultured the iMφ in the iAEO medium, growth was reduced and the iMφ lost their characteristic surface phenotype (Supplementary Fig. 2b, c). However, by carefully assessing the culture supplements in each growth medium, we successfully identified essential and detrimental factors for each cell type. We found that FBS was detrimental for iAEO survival (Supplementary Fig. 2d, e). However, iAEOs could survive and showed increased expression of SFTPA and CDC20 in the presence of FBS if the TGFβ inhibitor SB431542 was included in the growth medium (Supplementary Fig. 2f). Moreover, we observed that keratinocyte growth factor (KGF) was essential for preserving iAEO identity (data not shown), while expression of the surface marker CD14 was decreased in the presence of the GSK inhibitor CHIR99021 and dexamethasone (Supplementary Fig. 2g, h). Particularly, CHIR99021 significantly impacted iMφ identity. Based on these findings, we developed an RPMI-based co-culture medium, referred to as KSFM, which was supplemented with 2.5 ng/ml FGF7, 2.5 μM SB431542, 10% FBS, and 100 ng/ml M-CSF, and that supported maintenance of both iAEO and iMφ identities. In particular, KSFM is a medium that contains only low concentrations of SB431542 and KGF added to iMφ media. It can maintain similar functions, such as the expression of iMφ markers and the LPS response, comparable to those seen with iMφ-specific media (Supplemental

Fig. 2i). We also determined that the ratio of iAEOs and iMφ in co-cultures should be kept below 3:1, as a higher ratio of iMφ leads to increased levels of IL1β, potentially creating an environment similar to an inflammatory response (Supplementary Fig. 2j-k).

In the iAlvAssemb system, we observed homing of Alv-iMφ around Alv-iAEOs (Fig. 1h-k, Supplementary Fig. 1e and Supplementary Movie 1). Immunostaining confirmed cell type-specific markers, verifying that the cellular identity of Alv-iMφ and Alv-iAEOs is consistent within the iAlvAssemb system. (Fig. 1k). In addition, we detected elevated secretion of chemokines such as CCL3, CXCL10, CCL5, and CCL1 in the iAlvAssemb, as well as cytokines such as IL-6, IL1ra/IL1f3, and IL1b (Fig. 1l-o), indicating functional maturation of macrophages in the Alv-iAEOs niche, providing a dynamic and interactive cellular environment within the iAlvAssemb. Taken together, these findings demonstrated the successful establishment of the iAlvAssemb model.

Interactive communication with Alv-iAEOs and Alv-iMφ within iAlvAssemb

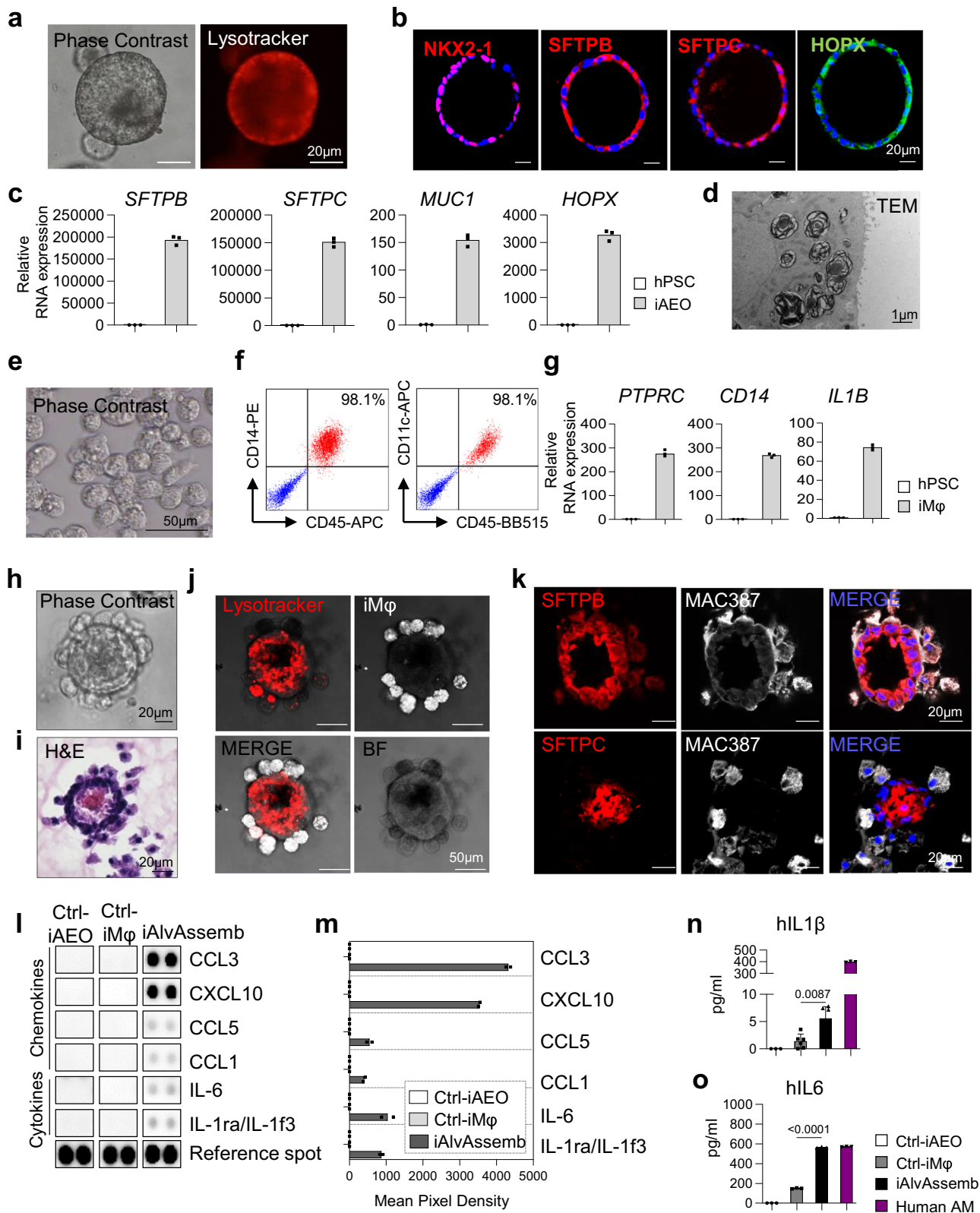
Next, we sought to investigate interactions between Alv-iAEOs and Alv-iMφ in the iAlvAssemb system using single-cell RNA sequencing (scRNA-seq) analysis. Cells were first grouped using unsupervised dimensionality reduction (t-SNE; t-Distributed Stochastic Neighbor Embedding) and then annotated using representative markers for each cell type (Fig. 2a-d and Supplementary Fig. 3). We found that the iMφ formed a single cell cluster, whereas the iAEO population was composed of three different clusters: AECs, proliferating AECs, and pulmonary neuroendocrine cells (Fig. 2a-d and Supplementary Fig. 3). The AECs includes both AT2-like cells and AT1-like cells (Supplementary Fig. 3). Interestingly, in the iAlvAssemb, Alv-iAECs and Alv-iMφ formed distinct clusters relative to the original cells, suggesting differential gene expression in these cells upon co-culture (Fig. 2a, b).

Differentially expressed genes (DEGs) analysis highlighted changes in both Mφ and AECs, with a larger number of DEGs observed in Mφ (Fig. 2e, f), indicating dynamic cell-cell interactions. Through Reactome pathway analysis, we identified an increase in genes related to macrophage functions, including interleukin signaling, trans-Golgi networks, chemokine signaling, and lipid metabolism. Additionally, we also observed an upregulation of genes associated with surfactant metabolism (Fig. 2f, g). Of particular interest, we found human AM-enriched genes such as *CD68*, *IL1b*, *CD163*, *ALOX5*, *MSR1*, and *MARCO* were upregulated in the iAlvAssemb cultures (Fig. 2h-i and Supplementary Fig. 1f), indicating the acquisition of an AM-like phenotype within the iAlvAssemb. Indeed, through flow cytometry analysis, we confirmed the increased expression of surface markers CD14, CD16 and CD163 (Fig. 2j, k and Supplementary Fig. 4), and using immunocytochemistry, we validated that expression of AM-specific markers (MSR1 and MARCO) were upregulated (Fig. 2l). Collectively, these data demonstrate that Alv-iMφ acquire an AM-like state in iAlvAssemb cultures.

An AM-like Tissue Adaptation of Alv-iMφ in the Alv-iAEO Niche

To investigate the molecular basis of the AM-like adaptation, we performed total RNA sequencing of ctrl-iMφ and isolated Alv-iMφ from iAlvAssemb (Fig. 3a, b). Overall, Gene Set Enrichment analysis (GSEA) revealed an enriched gene-signature of lung macrophage cells in Alv-iMφ compared to ctrl-iMφ (Fig. 3c).

To investigate Alv-iMφ' maturation, we performed a correlation analysis in which we compared gene expression changes in Alv-iMφ, Ctrl-iMφ, mono-Mφ, and HBAM (Human Alveolar macrophages from Bronchoalveolar lavage) (Fig. 3d). The analysis showed the highest correlation (Coefficient of Determination (R^2) = 0.5759) between Alv-iMφ and with HBAM (GSE174659). The sample distance matrix analysis also showed that Alv-iMφ were most closely located to HBAM, lending further supporting to Alv-iMφ undergoing an AM-like maturation (Fig. 3e). To assess the lung-specific adaptation of Alv-iMφ, we



compared it with previously reported RNA sequencing data of mouse lung (GSE63340) and identified 460 AM-enriched genes among the diverse tissue-resident macrophages. Through gene expression analysis of human orthologues, we then identified 180 genes that were upregulated in Alv-iMφ (Fig. 3f), and of those genes validated by RT-PCR that *IL1B*, *IL8*, *MSR1*, *ALOX5*, and *GPMB* gene expression was significantly increased (Fig. 3g and Supplementary Fig. 1f).

We were intrigued to see that mRNA levels of surfactant genes (typical markers of AT2 cells) increased in Alv-iMφ, but not in mono-Mφ or Ctrl-iMφ (Fig. 3f and Supplementary Fig. 5a–c), consistent with scRNA-seq data of human lung tissue (Supplementary Fig. 5d).

To assess functionality of Alv-iMφ, we examined phagocytosis and lipid uptake abilities of ctrl-iMφ and Alv-iMφ. We confirmed that phagocytosis was occurring in over 80% of cells in both groups, and

Fig. 1 | Characterization of iAEOs, iMφ, and iAlvAssemb. **a** Representative phase-contrast and lysotracker fluorescence images of iAEOs. Three independent experiment was repeated independently with similar results. **b** Representative immunostaining images showing the expression of the alveolar epithelial markers (NKX2.1, SFTPB, SFTPC, HOPX) in iAEOs. **c** Relative mRNA expression level of alveolar epithelial markers (*SFTPB*, *SFTPC*, *MUC1*, *HOPX*) in iAEOs and undifferentiated hESCs. Data were presented as mean ± SD, technical replicates ($n = 3$). **d** Representative TEM image showing lamellar bodies in iAEO. Two independent experiment was repeated independently with similar results. **e** Representative phase-contrast image of iMφ differentiated from hESCs. More than three independent experiment was repeated independently with similar results. **f** Representative flow cytometry plots of macrophage markers (CD45, CD14, CD11c) on iMφ. **g** Relative mRNA expression level of macrophage markers (*PTPRC*, *CD14*, *IL1β*) in iMφ and undifferentiated hESCs. Data were presented as mean ± SD with technical replicates ($n = 3$). **h–o** iAlvAssemb was created by co-culturing of iAEO

and iMφ in KSFM media for 7 days. More than three independent experiment was repeated independently with similar results. **h–i** Representative phase-contrast and H&E staining images of iAlvAssemb cultured in KSFM media. **j** Representative cell membrane-linked fluorescence images (Green) of iMφ and lysotracker fluorescence images (Red) of Alvi-iAEOs in AlviAssemb. **k** Representative immunostaining images showing the expression of the alveolar epithelial markers (SFTPB, SFTPC) and iMφ marker (MAC387) in AlviAssemb. **l, m** Cytokine blot array images and quantification of secreted cytokines in conditioned media of ctrl-iAEOs, ctrl-iMφ and iAlvAssemb cultured in KSFM media. **n, o** Quantification of IL1β and IL6 secretion in conditioned media of ctrl-iAEOs, ctrl-iMφ, iAlvAssemb and Human AM. Data were presented as mean ± SD with technical replicates for Ctrl-iMφ ($n = 6$), iAlvAssemb ($n = 6$), Ctrl-iAEO ($n = 3$), and Human AM ($n = 3$). Statistical analysis was performed using a one-way ANOVA with Dunnett's multiple comparisons test, and p -value (<0.05) was indicated on the graph.

that the ability to take up lipids was enhanced in Alvi-iMφ (Fig. 3h–i), indicating functional improvement.

Functional Response of Alvi-iMφ to Alveolar Damage

AMs feature highly characteristic thin and elongated pseudopodia that enable interaction with inhaled particles and microorganisms by extending into the alveolar space^{16,17}. We observed that Alvi-iMφ were capable of developing pseudopodia-like structures and contained lamellar bodies in the phagosome, indicating functional phagocytosis and recycling of surfactant lipids (Fig. 4a).

To evaluate whether the AlviAssemb platform could replicate in vivo cellular function, we induced alveolar epithelial injury using bleomycin. After 48 h of treatment, expression of damage-response genes, including *p21*, *BAX*, and *ISG15*, was upregulated in Ctrl-iAEOs, Ctrl-iMφ, and iAlvAssemb (Fig. 4b). However, using live/dead staining and immunostaining for the cleaved Caspase 3, we detected significantly fewer dead cells in the iAlvAssemb than in the Ctrl-iAEOs only (Fig. 4c and Supplementary Fig. 6), suggesting that Alvi-iMφ effectively removes damaged alveolar cells in the iAlvAssemb, a crucial in vivo function of AMs in tissue homeostasis. To validate this capability, we stained for oxidized lipids given that AMs are known to take up oxidized lipids produced from dead cells¹⁸. Our data demonstrate that oxidized lipids were indeed present in damaged AECs in Ctrl-iAEOs, but not in Alvi-iMφ. In contrast, the Alvi-iMφ in the iAlvAssemb exhibited an oxidized lipid signal, indicating uptake of oxidized lipids in Alvi-iMφ during phagocytic clearance of damaged debris (Fig. 4d). Overall, these findings suggest that Alvi-iMφ are structurally and functionally mature and that the iAlvAssemb represent a promising cellular platform for investigating functional human cell-cell interactions known to occur in vivo.

GM-CSF, a paracrine for tissue adaptation of Alvi-iMφ

To investigate the factors contributing to tissue adaptation of iMφ in the iAlvAssemb, we established a parabiotic organoid culture system in which iAEOs and iMφ are sharing the same media but cultured in separate matrigel domes within the same dish (Fig. 5a). In this setup, we detect upregulation of Alvi-iMφ-enriched genes (*ALOX5*, *MSR1*, *CCL4*, *IL1b*, and *IL8*) in the para-iMφ, indicating that the presence of iAEO-derived paracrine factors regulate the tissue adaptation of iMφ (Fig. 5b).

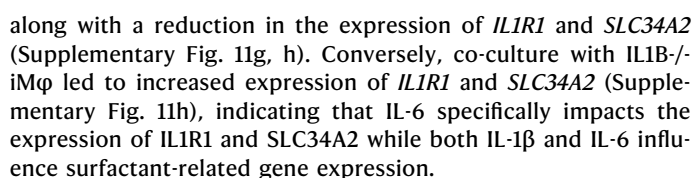
We detected high expression of GM-CSF in SFTPC⁺ alveolar type 2 cells (AT2) by scRNA-seq (Fig. 5c). Using cytokine array analysis, we documented that GM-CSF is secreted in both iAEOs and iAlvAssemb, and confirmed by RT-PCR that the GM-CSF receptor (*CSF2RA*) was expressed in both Ctrl-iMφ and iAlvAssemb (Fig. 5d, e). When we treated Ctrl-iMφ with GM-CSF (but not G-CSF), we found that expression of Alvi-iMφ-enriched genes was increased (*ALOX5*, *MSR1*, *CCL4*, *IL1b*, and *IL8*) (Fig. 5f, g). Immunostaining confirmed increased expression of MSR1, a marker

specific to AMs, as well as enhanced lipid uptake by GM-CSF treatment (Fig. 5h, i and Supplementary Fig. 7a, b). Moreover, by applying a GM-CSF blocking antibody, we could partially inhibit the upregulation of Alvi-iMφ-enriched genes in the iAlvAssemb (Supplementary Fig. 7c). To clarify the role of GM-CSF in Alvi-iMφ adaptation, we created CSF2^{-/-} iAEOs through CRISPR/Cas9-based gene editing (Supplementary Fig. 8a–c and Fig. 6a–d) and verified the absence of GM-CSF secretion using enzyme-linked immunosorbent assay (ELISA) (Fig. 5l). When iMφ were co-cultured with CSF2^{-/-} iAEOs, gene expression for *IL1b*, *IL8*, *CCL4*, and *ALOX5*, typically elevated in Alvi-iMφ due to interaction with iAEOs, was not increased (Fig. 6f, g). Furthermore, lipid uptake was reduced in Alvi-iMφ co-cultured with CSF2^{-/-} iAEOs (Fig. 6h, i), indicating a significant role of GM-CSF in the tissue adaptation of Alvi-iMφ in iAlvAssemb.

However, the surfactant-related genes that were confirmed to be increased in Alvi-iMφ in Supplementary Fig. 4c were not elevated by GM-CSF treatment (Supplementary Fig. 9a). Instead, a significant amount of SFTPC mRNA was observed in exosomes secreted from Ctrl-iAEOs (Supplementary Fig. 9b, c). This suggests that the SFTPC mRNA detected in Alvi-iMφ may result from exosome delivery from AT2 cells to Alvi-iMφ. These findings are consistent with the observation of SFTPC mRNA in various non-parenchymal cells, such as macrophages and endothelial cells, in human lung tissue (Supplementary Fig. 4d), which might imply exosome-mediated cell interaction.

Interleukins-mediated surfactant regulation in AECs

In the iAlvAssemb t-SNE plot, we noted a distinct cluster of AECs, reflecting significant gene expression changes resulting from interactions with Alvi-iMφ (Fig. 7a). Upregulated genes were associated with interleukin signaling, immune system, and chemokine signaling pathways (Supplementary Fig. 10a–d). Additionally, we detected an increase in genes related to surfactant metabolism, including *SFTPA1* and *SFTPA2* (Fig. 7b–d), without any change in the expression of markers for AT1 cells (Fig. 7e). We validated these gene alterations by RT-PCR (Fig. 7f), and noted similar gene expression increases in indirect parabiotic organoids culture (Fig. 7g, h), suggesting that paracrine signaling instructs these gene expression changes. Notably, we found that IL-1β and IL-6 treatment led to upregulation of both *SFTPA1* and *SFTPA2* in a concentration-dependent manner (Fig. 7i). Conversely, at higher concentrations, both IL-1β and IL-6 inhibited SFTPC expression. The iMφ differentiated from IL1B^{-/-} or IL6^{-/-} hESCs exhibited increased IL-6 secretion in IL1B^{-/-} iMφ, and vice versa, likely due to functional compensation between these cytokines (Supplementary Fig. 11a–f). In the co-culture with IL6^{-/-} iMφ, which lacked IL-6 but showed increased IL-1β levels, there was a significant increase in the expression of surfactant genes *SFTPA1*, *SFTPC*,



To assess iAlvAssemb's capability to model immune responses resulting from lung infection, we performed scRNA-seq analysis after LPS response. In t-SNE analysis, we noted distinct clustering of macrophages and ILIR1⁺ AECs in LPS-treated vs. non-treated iAlvAssemb

Fig. 2 | Transcriptional regulation of iAlvAssemb system. scRNA-seq was performed with ctrl-iAEOs and iAlvAssemb grown in KSFM media with biological replicates ($n = 2$), and Data was integrated with iMφ data (GSE133935), previously reported. **a**, **b** The t-SNE plot represents the clustering of cell populations based on cell type-specific markers (**a**) and Library ID (**b**). **c**, **d** Violin plot and heatmap represents the log₂-transformed expression values of cell-type specific markers, including a box plot that highlights the interquartile range (IQR), median, and mean (horizontal line). **e** Venn diagram showing the numbers of DEGs in both Mφ and AECs. **f** Heatmap of DEGs in both Mφ and AECs. **g**, Representative enriched pathway in DEGs of Mφ and AECs. **h** Violin plots showing log₂-transformed expression values

of Alv-iMφ-enriched genes, includes a box plot highlighting the interquartile range (IQR), median and mean (horizontal line). **i** t-SNE plot showing the expression of Alv-iMφ-enriched genes in iAlvAssemb system and human lung tissues. **j–l** ctrl-iMφ, ctrl-iAEO and iAlvAssemb was grown in 50% GFR-matrigel with KSFM medium for 7days. **j**, **k** Representative flow cytometry dot-plots and quantitative analysis of macrophage-specific surface markers in ctrl-iMφ, and Alv-iMφ isolated from iAlvAssemb. Data were presented as mean \pm SD with technical replicates ($n = 3$). **l** Representative immunostaining images showing the expression of the alveolar marker (MUC1) and AM-specific markers (MARCO, MSR1). Two independent experiment was repeated independently with similar results.

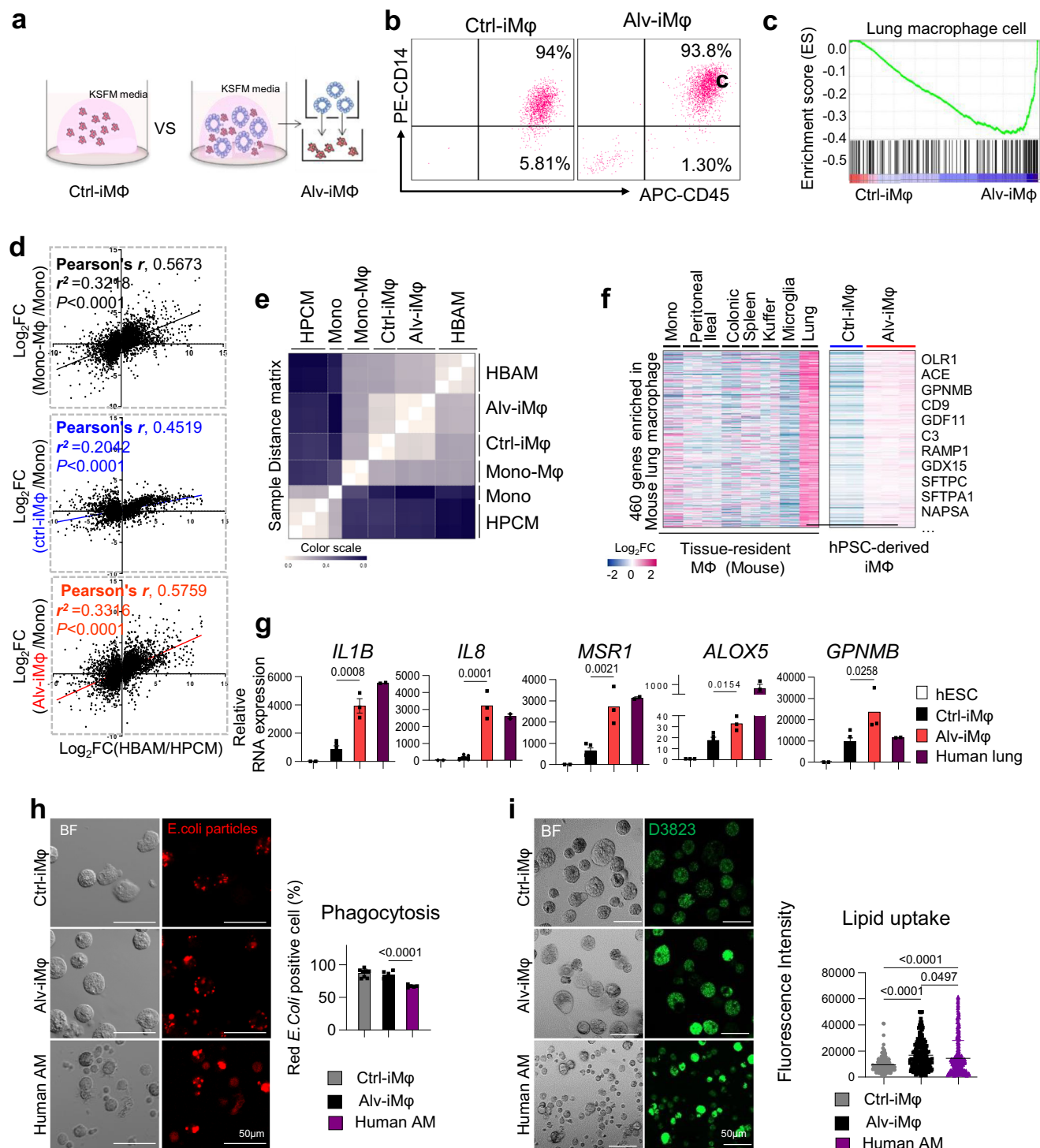


Fig. 3 | Tissue adaptation and maturation of iMφ in iAlvAssemb system. Ctrl-iMφ and iAlvAssemb was grown in 50% GFR-matrigel with KSFM medium for 7 days and Alv-iMφ was isolated from iAlvAssemb. **a** Schematic images showing the method to isolate Alv-iMφ from iAlvAssemb. **b** Representative flow cytometry plots of macrophage markers (CD14, CD45) on Ctrl-iMφ and Alv-iMφ. **c** GSEA-enrichment plot showing gene signature of lung macrophage cells on Ctrl-iMφ and Alv-iMφ. **d** A scatter plot showing the correlation of gene expression ($n = 7080$) between induced macrophages (Mono-Mφ, Ctrl-iMφ, Alv-iMφ) and tissue-resident alveolar macrophages (HBAM, original dataset from GSE174659), normalized relative to monocytes. correlation coefficient (**Pearson's r**) and p value was presented in figures. **e** Sample Distance matrix of indicated samples. **f** Heatmap of mouse AM-specific gene clusters in the lung from transcriptome data of macrophages in various tissues (left panel, original dataset: GSE63340), Heatmap showing the relative expression of human orthologs of mouse AM-specific genes in ctrl-iMφ and alv-iMφ

(right panel). **g** Relative mRNA expression level of significantly increased genes in undifferentiated hESC, Ctrl-iMφ, Alv-iMφ, and human lung. Alv-iMφ was isolated from iAlvAssemb. Data were presented as mean \pm SD. Statistical analysis was performed using an unpaired t-test between Ctrl-iMφ ($n = 5$) and Alv-iMφ ($n = 3$), biological replicates. P -value (<0.05) was indicated on the graph. **h** Representative phase-contrast, fluorescence images and quantifications showing phagocytosis ability. Data presented as mean \pm SD with technical replicates; Ctrl-iMφ ($n = 8$), Alv-iMφ ($n = 6$), and Human AM ($n = 5$). Human AM (ACCEGEN) were cultured in Human alveolar macrophage media for experimental control. **i** Representative phase-contrast and lipid analogues (D3823, Green) fluorescence images, and quantifications showing lipid uptake ability. Data were presented as mean \pm SD with technical replicates; Ctrl-iMφ ($n = 219$), Alv-iMφ ($n = 185$) and Human AM ($n = 1058$). Statistical analysis was performed using a one-way ANOVA with Dunnett's multiple comparisons test, and p -value (<0.05) was indicated on the graph.

(Fig. 8a–f). Amongst DEGs, we found 37 common alterations in AECs and Mφ, suggesting shared changes in antigen presentation, ER-phagosome pathway, and interferon signaling (Fig. 8g–i, and Supplementary Fig. 12a, b). Some cytokines, chemokines, and surface molecules like as *IL6*, *IL1B*, *CXCL11*, *CXCL9*, *CD38*, *CD274*, *SLAMF7* were upregulated only in Alv-iMφ (Fig. 8j–l), while in AECs, *IL32* expression was altered and expression of AT1 cell markers (*HOPX*, *AQP4*, *CLIC5* and *AGER*) was reduced (Fig. 8m). Notably, there was a significant decrease in the expression of ribosomal proteins and translation-related genes in Alv-iMφs, but not in AECs (Fig. 8i and Supplementary Fig. 12c), suggesting a possible differential regulation of cell type-specific translation by infection,

We also found that expression of pathogen entry receptors was altered in co-culture of iAEOs and iMφ (Supplementary Fig. 13a and S13b). Specifically, in Alv-iMφ, we detected and validated by RT-PCR increased expression of CD44 (Supplementary Fig. 13c, d), a cell surface glycoprotein that mediates recruitment of inflammatory cells and that is a macrophage binding site for *Mycobacterium tuberculosis* (M.tb). We also show that CD44 is upregulated in response to GM-CSF stimulation (Supplementary Fig. 13e). To model infection in the iAlvAssemb platform, we employed fluorescence-tagged M.tb (H37Rv) and examined whether iMφ were permissive for M.tb (H37Rv) from a multiplicity of infection (MOI), ranging from 1 to 20 bacteria per cell, in a dose-dependent manner. We found that the highest infection led to effective intracellular replication (Supplementary Fig. 14), demonstrated that the virus preferentially infected iMφ (Supplementary Fig. 13f–g), consistent with its known in vivo tropism for AM as primary targets. Infection efficiency was even higher in isolated Alv-iMφ (Supplementary Fig. 13h, i), emphasizing the relevance of AM in M.tb infection. To leverage the iAlvAssemb model system for M.tb infection, we measured cellular fate decision, a hallmark of M.tb intracellular replication. iMφ and Alv-iMφ underwent apoptosis and necrosis upon M.tb infection and, Alv-iMφ were more sensitive to the M.tb infection resulting in a high level of necrotic cell death compared to iMφ (Supplementary Fig. 15a, b). To extend our understanding of the necrotic cell death, we analyzed metabolic activity in Alv-iMφ, and found that the major cellular energy-producing metabolisms such as glycolysis and oxidative phosphorylation were decreased in the Alv-iMφ by M.tb infection (Supplementary Fig. 15c–g) which recapitulated the metabolic responses of mono-Mφ. Taken together, these findings support that iAlvAssemb can be leveraged as human disease-relevant model system to investigate inflammation and respiratory infectious disease¹³, offering insights into lung microenvironment tropism and infection dynamics.

Discussion

Our study makes a significant stride towards modeling the intricate cellular dynamics within the human lung environment, and specifically focusing on the interactions between AECs and AMs. By leveraging organoid technology, we derived both iAEOs and iMφ from hPSCs, and

successfully established the iAlvAssemb system, which incorporates functional macrophages. Our advance opens up new avenues for modeling human lung infection and disease, gaining novel insights that could inform the development of therapeutic strategies for lung diseases, and testing compounds for efficacy in preclinical disease paradigms.

We found that both iAEOs and iMφ, when co-cultured in the iAlvAssemb model, underwent distinct changes, highlighting how their interactive milieu intricately influences and shapes both cellular identity and function. Our work also underlines the importance of carefully designing and optimizing a co-culture medium capable of sustaining the unique identities of both cell types, an instrumental component of setting up the iAlvAssemb. Importantly, we demonstrate that the iAlvAssemb exhibits cellular characteristics and interactions akin to those of lung tissue, as evidenced by our data showing that the iMφ acquired a global gene expression profile similar to human tissue macrophages and upregulated specific genes known to be upregulated in human AMs. Our finding aligns well with the tissue adaptation of macrophages, in which the tissue environment shapes the identity and function of macrophages^{19,20}. Interestingly, we also observed an increase in the expression of surfactant genes in Alv-iMφ, suggesting that AMs not only contribute to surfactant clearance but also play a role in its production. Collectively, the iAlvAssemb provides a versatile platform for studying macrophage biology within a tissue-like context, facilitating investigations into their functions and contributions to pulmonary physiology and disease.

A significant finding was the Alv-iMφ were capable of executing functional phagocytosis and lipid uptake, and that they were morphologically similar to AM. Our data demonstrate that the Alv-iMφ remove damaged alveolar cells and absorb oxidized lipids, validating the iAlvAssemb's potential in modeling diseases associated with macrophage dysfunction or alveolar damage. These functional data are particularly significant given the role of macrophages in maintaining homeostasis in lung tissue and their involvement in various lung diseases.

Our study also noted the impact of paracrine factors, and particularly GM-CSF expressed by AT2-like cells in iAEOs, in influencing the characteristics of Alv-iMφ. This observation unveils a potential mechanism through which epithelial-macrophage interactions could dictate the characteristics and functions of AMs within the human lung. Interestingly, the importance of GM-CSF in mouse AM development was previously reported in a study on fetal lung development, further supporting the significance of this interaction^{21,22}. Additionally, we observed that co-culture with iMφ led to changes in expression of genes related to epithelial cell defense in iAEOs, and particularly increased levels of surfactant protein A (SFTPA), an essential component of the lung's innate immune response^{23,24}. Intriguingly, we demonstrate mechanistically that the changes in iAEOs were mediated by interleukin-1b and interleukin-6 secreted by Alv-iMφ, shedding light on how macrophages shape the functional characteristics of AECs.

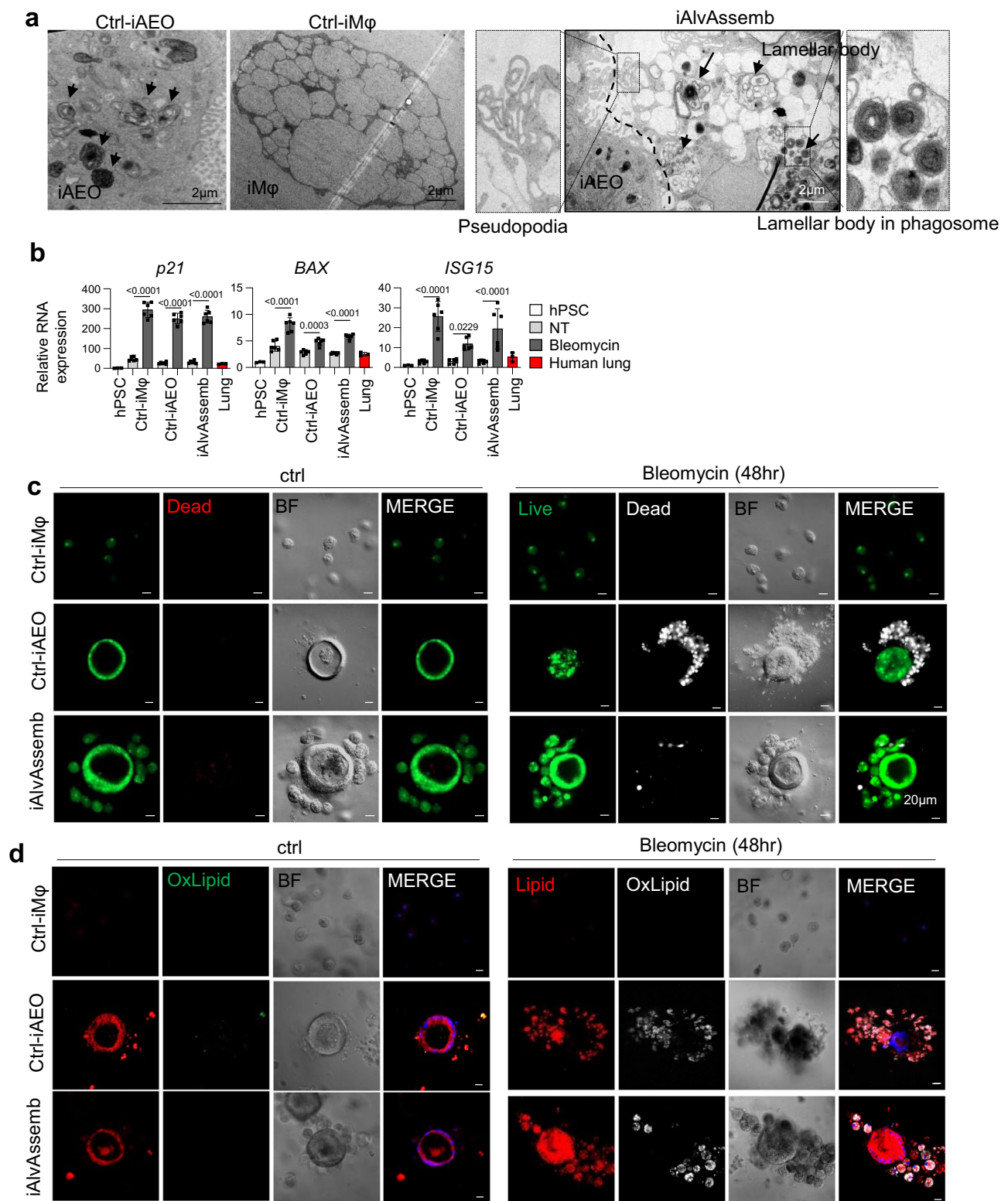


Fig. 4 | Phagocytic clearance of damaged AECs by Alv-iMφ. a Representative TEM images of Ctrl-iAEOs, Ctrl-iMφ, and iAlvAssemb cultured in KSFM media. The left panel shows Ctrl-iAEO with lamellar bodies indicated by solid arrows, while the middle panel presents Ctrl-iMφ. In iAlvAssemb (right panel), iAEO is positioned on the left side of the dashed line, with the recruited iMφ on the right. An inset on the left highlights the extended pseudopodia in iAlvAssemb, while another on the right shows lamellar bodies within the phagosome of iMφ. **b** Relative mRNA expression level of damage-response genes (*p21*, *BAX*, *ISG15*) by bleomycin treatment for 48 h.

Data were presented as mean \pm SD with technical replicates; Ctrl-iMφ, Ctrl-iAEO, iAlvAssemb ($n = 6$). Statistical analysis was performed using a two-way ANOVA with Sidak's multiple comparisons test, and p -value (<0.05) was indicated on the graph. **c** Representative phase-contrast and live (Green)/dead (Red) fluorescence images by bleomycin treatment for 48 hr in Ctrl-iMφ, Ctrl-iAEOs, and iAlvAssemb. **d** Representative phase-contrast and peroxidation lipid (Green)/normal lipid (Red) fluorescence images by bleomycin treatment for 48 h in Ctrl-iMφ, Ctrl-iAEOs, and iAlvAssemb.

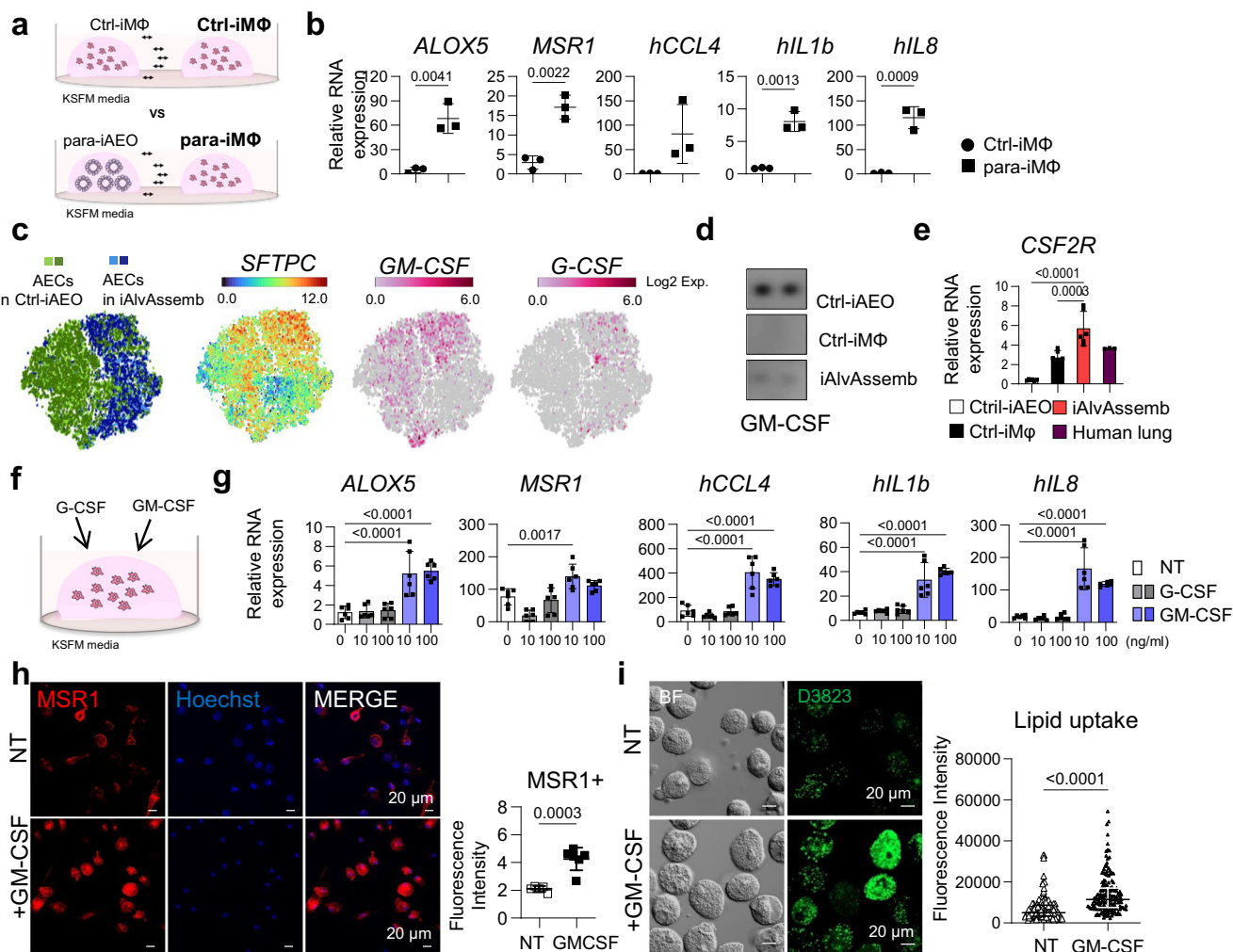


Fig. 5 | Paracrine effects of GM-CSF in iAlvAssemb system. **a** A schematic explanation of parabolic organoid culture systems. **b** Relative mRNA expression level of Aliv-iMφ-enriched genes (*ALOX5*, *MSR1*, *CCL4*, *IL1β*, *IL8*) in the Ctrl-iMφ and Aliv-iMφ of parabolic organoid system. Data were presented as mean ± SD with biological replicates ($n = 3$). Statistical analysis was performed using an unpaired t-test, and p -value (<0.05) was indicated on the graph. **c** Gene expression of *SFTPC*, *GM-CSF* and *G-CSF* in the AECs in Ctrl-iAEO and iAlvAssemb on t-SNE plot of scRNA-seq analysis. **d** Representative cytokine blot array images of GM-CSF in conditioned media of Ctrl-iAEOs, Ctrl-iMφ and iAlvAssemb. **e** Relative mRNA expression level of *CSF2R* in Ctrl-iAEOs, Ctrl-iMφ, iAlvAssemb and human lung. Data were presented as mean ± SD with biological replicates ($n = 6$) for Ctrl-iAEOs, Ctrl-iMφ, iAlvAssemb and statistical analysis was performed using a one-way ANOVA with Dunnett's

multiple comparisons test. p -value (<0.05) was indicated on the graph. **f** A schematic explanation of G-CSF or GM-CSF treatment on Ctrl-iMφ. **g** Relative mRNA expression level of Aliv-iMφ-enriched genes in Ctrl-iMφ with or without treatment of G-CSF and GM-CSF at 10 or 100 ng/ml for 7 days. Data were presented as mean ± SD with technical replicates ($n = 6$) and statistical analysis was performed using a one-way ANOVA with Dunnett's multiple comparisons test. p -value (<0.05) was indicated on the graph. **h**, **i** Representative immunostaining images showing the expression of AM specific marker (MSR1, Red) and lipid uptake (D3823, Green) in iMφ with or without 100 ng/ml of GM-CSF, and quantification of the F.I. Data were presented as mean ± SD with technical replicates; n (**h**) = 5, n (**i**) = 159. Statistical analysis was performed using an unpaired t-test, and p -value (<0.05) was indicated on the graph.

Furthermore, our study demonstrated that iAlvAssemb generate an immune response in response to LPS stimulation, suggesting utility as a 3D cellular in vitro model for studying the lung immune response to a bacterial infection. The LPS-induced changes in chemokines and cytokines we annotated, along with distinct clustering patterns and altered gene expression profiles in macrophages and AECs, serve as benchmarks against which other infectious agents or co-administered therapeutic agents can be investigated in the iAlvAssemb model. To this end, we demonstrate the ability of iAlvAssemb to recapitulate the cellular tropism observed in *M.tb* infection, a significant step towards establishing a robust in vitro model for studying lung infections. Taken together, we propose that iAlvAssemb is capable of replicating aspects of the elusive immune responses of the human lung, thereby making it a valuable research platform for studying cell-specific defense responses and their interactions.

In conclusion, we here describe the iAlvAssemb platform, a model that enables understanding cellular interactions representative of the human lung environment and mechanistic interrogations of macrophage-mediated immune responses. By combining iAEOs and iMφ in a dynamic tissue environment, iAlvAssemb enables disease modeling studies of the complex interplay between AECs and AMs, interrogations of downstream mechanisms impacting on cellular identity and function, and development of therapeutic strategies for lung diseases. Despite these significant advances, we recognize that our model does not encompass other cell types that also contribute to lung tissue function, such as fibroblasts, endothelial cells, and diverse immune cells. Furthermore, the detailed mechanisms of which types of iMφ participate in homing and what factors induce homing remain unknown. Future efforts are needed to further refine iAlvAssemb to better replicate the highly complex lung tissue, along with more sophisticated analyses of cell-cell interactions.

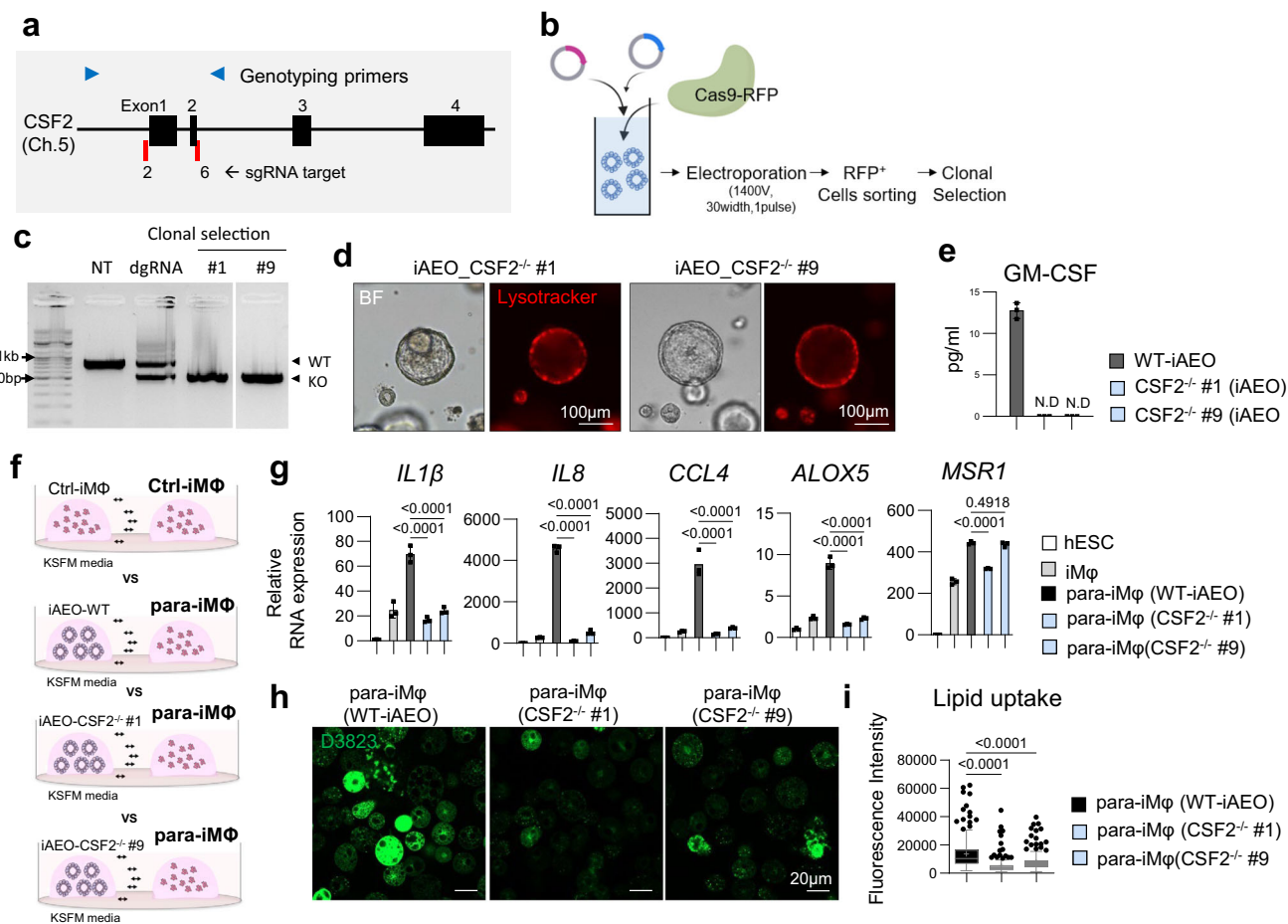


Fig. 6 | The role of GM-CSF on the tissue adaptation of Alveolar Epithelial Organoids (iAEO) from hPSCs. **a** Illustration of genomic DNA showing target of the dual guide RNA and genotyping primers used to produce CSF2^{-/-} iAEO. **b** Schematic image showing the strategy for CSF2^{-/-} iAEO generation. **c** Agarose gel electrophoresis of PCR amplified products for CSF2 genotyping. **d** Phase contrast images and fluorescence images for Lysotracker staining of CSF2^{-/-} iAEO lines cultured in iAEO media. **e** Quantification of GM-CSF secretion in conditioned media of WT-, CSF2^{-/-} iAEO #1, and #9 lines cultured in KSFM media. Data are presented as mean ± SD with technical replicates (*n* = 3). ND, not detected. **f** Schematic images showing the parabolic organoid cultures of iMφ with Ctrl-iMφ, wt-iAEO or CSF2^{-/-} iAEO in KSFM media for 7 days. **g** Relative

mRNA expression level of Alveolar Epithelial Organoid (iAEO)-enriched genes (*IL1β*, *IL8*, *CCL4*, *ALOX5* and *MSR1*). Data presented as mean ± SD with technical replicates (*n* = 3). Statistical analysis was performed using a one-way ANOVA with Dunnett's multiple comparisons test, and *p* value (<0.05) was indicated on the graph. **h**. Representative fluorescence images showing the lipid uptake (D3823, Green) in para-iMφ with WT-, CSF2^{-/-} iAEO #1, and #9. **i**. Quantification of the F.I. Data were presented as mean ± SD with technical replicates; WT (*n* = 209), #1 (*n* = 180) and #9 (*n* = 224). Statistical analysis was performed using a one-way ANOVA with Dunnett's multiple comparisons test, and *p*-value (<0.05) was indicated on the graph.

Methods

Human pluripotent stem cells (hPSCs)

In this study, one hESC lines (H9) and one hiPSC (CRL2-iPSC) were used. hESCs (H9) were obtained from the WiCell Research Institute (WiCell, Madison, WI) and hiPSC were reprogrammed from skin fibroblast (ATCC, Manassas, VA) by episomal vector. hPSCs were maintained in mTeSR-1 medium (STEMCELL™ Technologies, Vancouver, Canada) and subcultured with ReLeSR (STEMCELL™ technologies) as following manufacturer's instructions. This study was approved by Korean Public IRB (No. P01-2014-ES-01-09, and P01-201609-31-002).

Differentiation and maintenance of Alveolar Epithelial Organoids (iAEO) from hPSCs

iAEOs were differentiated from hPSCs by previously reported^{10,25}, with modifications. Briefly, hPSCs were grown in 1% matrigel (Corning, N.Y.)-coated dish with the mTeSR-1 medium. To differentiate into definitive endoderm, hESC were dissociated into single cells using Accutase and transferred to matrigel-coated dishes at a density of 2 × 10⁵ cells/cm². Cells were cultured for 24 h in mTeSR-1 medium with 10 μM Y27632 (R&D Systems, Minneapolis, MN, USA), and

differentiated into definitive endoderm by using STEMdiff™ Definitive Endoderm Kit (STEMCELL™ technologies) for 72 h. For anterior foregut specifications, definitive endoderm cells were transferred to matrigel-coating dish with 1:4 split and exposure to 2 μM dorsomorphin (Sigma-Aldrich, Burlington, MO) and 10 μM SB4531542 (Tocris Bioscience, Bristol, UK) in SFM medium (75% IMDM, 25 % Ham's F12, 0.5X N2, 0.5X B27, 0.056% BSA, 1% P/S, 1% Glutamax, 50 μg/ml Ascorbic Acid, 0.4 μM Monothiolglycerol) for 72 h. Then, Lung endoderm cells were induced by SFM medium supplemented with 3.5 μM CHIR 99021 (Tocris), 10 ng/ml hrBMP4 (R&D Systems) and 100 nM Retinoic Acid (Sigma-Aldrich) in cells on day9. On differentiation day 15, cells were detached into small clumps by treatment of Gentle Cell Dissociation Reagent (STEMCELL™ technologies), and embedded matrigel dome in the SFM medium supplemented with 3.5 μM CHIR 99021, 10 ng/ml FGF7 (R&D Systems), 10 ng/ml FGF10 (R&D Systems), 500 nM Retinoic Acid. Seven days later, NKX2.1 positive cells were sorted by FACSARIA™ III Cell Sorter (BD Biosciences, San Jose, CA) for the CD26-PE/CD47-PerCP Cy5⁺ cells and re-embedded in a matrigel dome. Further differentiation into AECs, cells were differentiated by SFM medium supplemented with 3.5 μM CHIR9921, 10 ng/ml FGF7, 50 nM Dexamethasone (Sigma-Aldrich), 100 μM 8-br-cAMP (Biolog, Hayward,

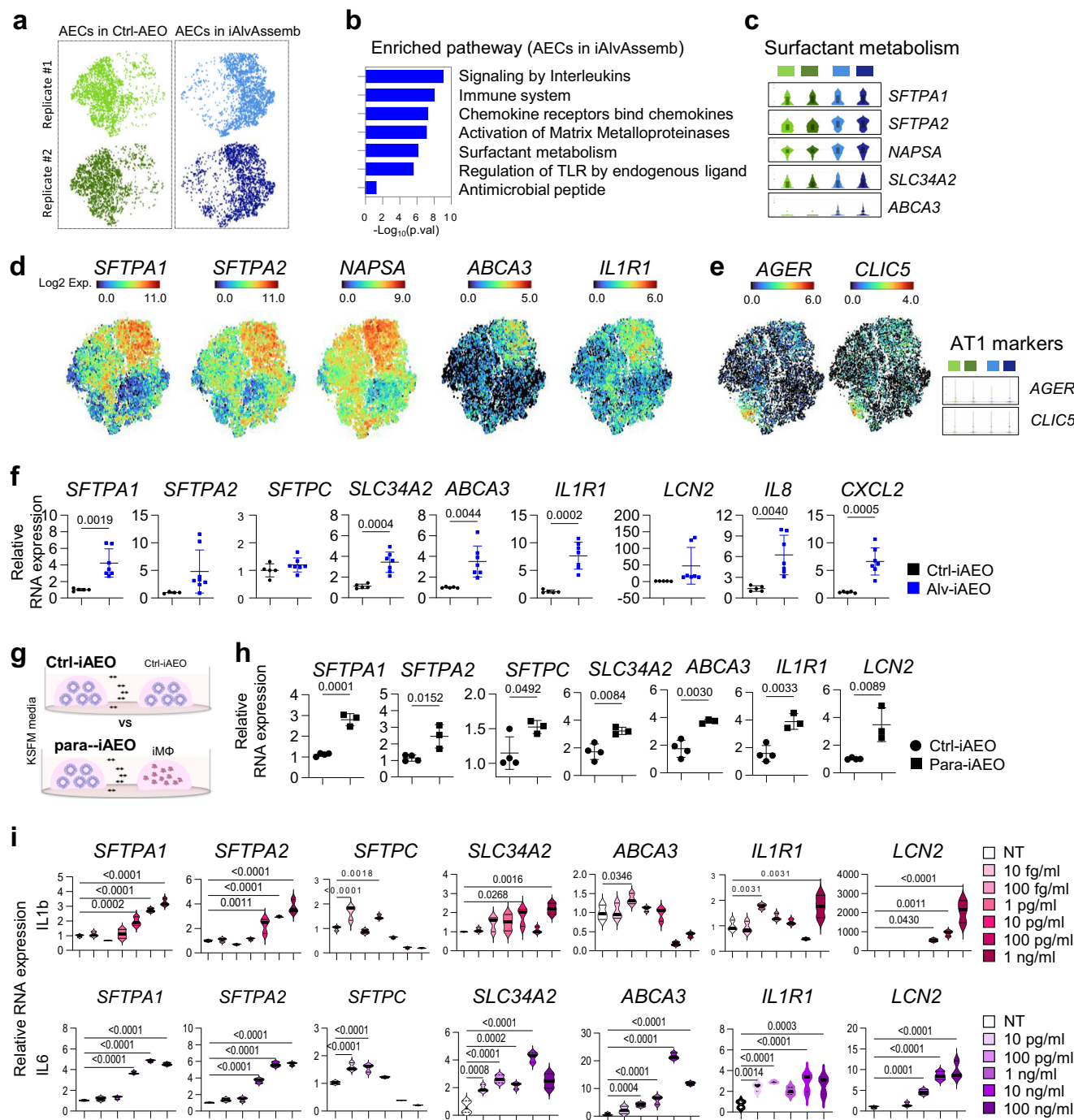


Fig. 7 | Paracrine effects of interleukin to Alveolar Epithelial Cells (AECs). **a** t-SNE plots showing single cell distribution of individual replicates in Ctrl-iAEOs and Alveolar Epithelial Cells (AECs).

b, c Representative enrichment pathways in DEG analysis and Violin plots showing log expression level of surfactant metabolism related genes of Alveolar Epithelial Cells (AECs). Each violin includes a box plot showing the interquartile range (IQR), with horizontal lines indicating the median and mean. **d, e** Expression of genes related with AT2 cells (*SFTPA1*, *SFTPA2*, *NAPSA*, *ABCA3* and *IL1R1*) (**d**) and AT1 cells (*AGER*, *CLIC5*) (**e**) on t-SNE. **f** Relative mRNA expression level of surfactant metabolism (*SFTPA1*, *SFTPA2*, *SFTPC*, *SLC34A2* and *ABCA3*) and immune related genes (*IL1R1*, *LCN2*, *IL8* and *CXCL2*) in Ctrl-iAEOs and Alveolar Epithelial Cells (AECs) isolated from iAlvAssemb cultured in KSMF media. Data were presented as mean \pm SD with biological replicates; Ctrl-iAEO ($n = 5$), Alveolar Epithelial Cells (AECs) ($n = 7$). Statistical analysis was performed using an unpaired t-test,

and p -value (<0.05) was indicated on the graph. **g, h** A schematic explanation (**h**) of paracrine culture of iAEOs with iMφ in KSMF media for 7 days. **h** Relative mRNA expression level of surfactant metabolism (*SFTPA1*, *SFTPA2*, *SFTPC*, *SLC34A2* and *ABCA3*) and immune related genes (*IL1R1* and *LCN2*) in Ctrl-iAEO and para-iAEO. Data were presented as mean \pm SD with biological replicates; Ctrl-iAEO ($n = 4$), Para-iAEO ($n = 3$). Statistical analysis was performed using an unpaired t-test, and p -value (<0.05) was indicated on the graph. **i** Relative mRNA expression level of surfactant metabolism (*SFTPA1*, *SFTPA2*, *SFTPC*, *SLC34A2* and *ABCA3*) and immune related genes (*IL1R1* and *LCN2*) in iAEOs with or without IL1 β or IL6 in KSMF media for 7 days. Data were presented as mean \pm SD with technical replicates ($n = 3$). Statistical analysis was performed using a one-way ANOVA with Dunnett's multiple comparisons test, and p -value (<0.05) was indicated on the graph.

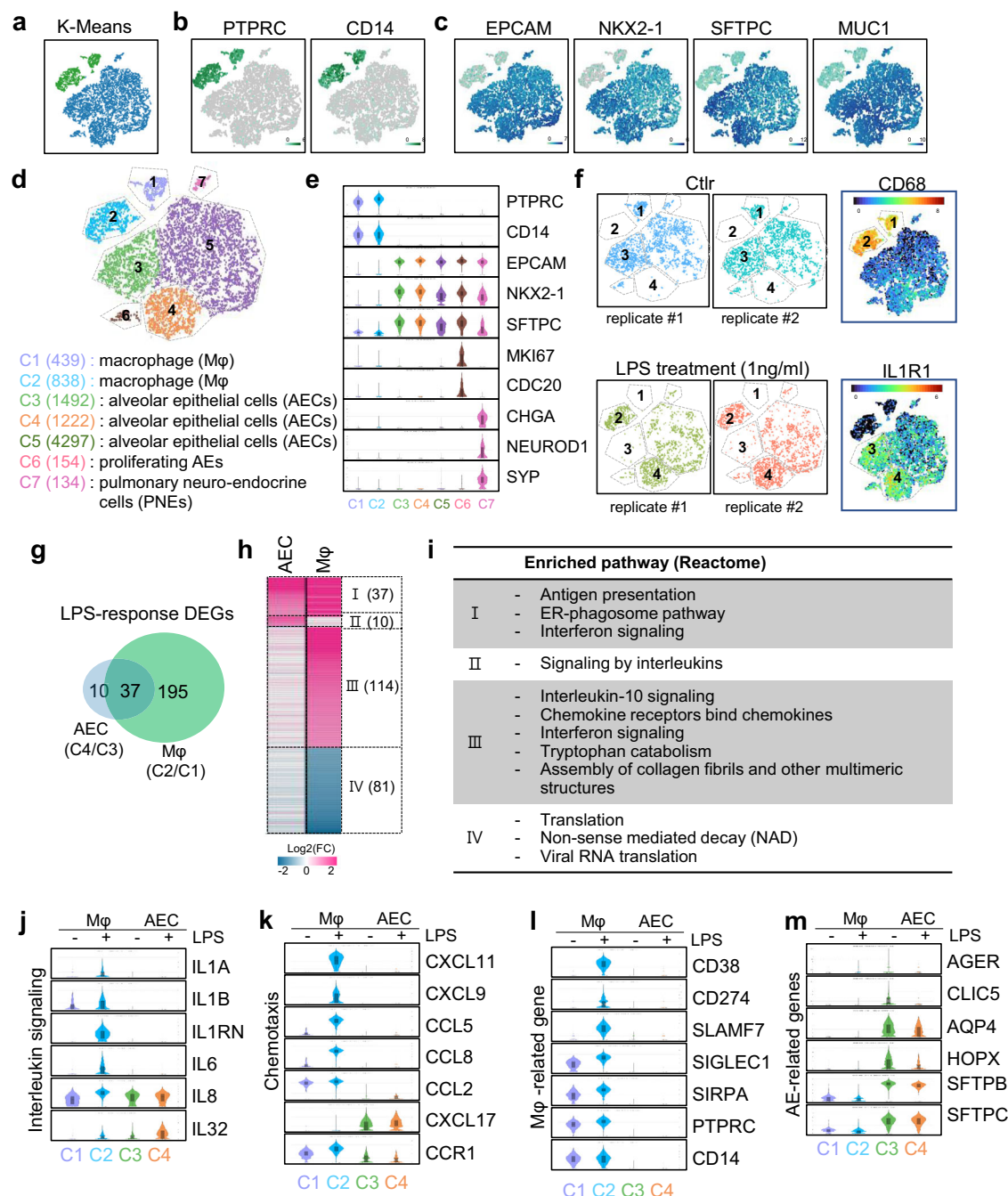


Fig. 8 | iAlvAssemb as a disease modeling system with LPS. **a** t-SNE Plot of Merged iAlvAssemb with and without 1 ng/ml LPS Treatment for 24 h in KSFM media (K-means clustering). **b**, **c** t-SNE Plot showing the expression of genes related with macrophage (*PTPRC*, *CD14*) and alveolar epithelial markers (*EPCAM*, *NKX2-1*, *SFTPC*, *MUC1*). **d** Cell clustering and cell type annotation of iAlvAssemb system. **e** Violin plots showing the log gene expression of cell type specific markers in each cluster. Each violin includes a box plot showing the interquartile range (IQR), with horizontal lines indicating the median and mean. **f** t-SNE plots showing the

difference in cell clusters based on library id, and expression of CD68 and IL1R1. **g**, **h** Venn diagram and heatmap of DEG analysis with LPS-response in AEC and iMφ. **i** List of enriched Reactome Pathways in iAlvAssemb after LPS treatment. **j**–**m** Violin plots showing gene expression related with interleukin signaling (**j**), chemotaxis (**k**), Mφ (**l**) and AEC-specific markers (**m**) after LPS treatment. Each violin includes a box plot showing the interquartile range (IQR), with horizontal lines indicating the median and mean.

CA), 100 μM IBMX (Sigma-Aldrich). On days 30–35, CHIR9921 was withdrawn and later it was added back. To enrich iAEOs were differentiated from hESCs by previously reported iAEOs were differentiated from hESCs by previously reported iAEO, the organoids were selectively cultured to identify clones that stained positively with Lyso-tracker after low-density single-cell seeding. For long-term maintenance, organoids were cultured in a matrigel dome with SFM medium supplemented with 3.5 μM CHIR9921, 10 ng/ml FGF7, 50 nM

Dexamethasone, 100 μM 8-br-cAMP, 100 μM IBMX, and 10uM SB431542, and passaged by small clump every 2weeks.

Differentiation and maintenance of iMφ from hPSCs

Differentiation of iMφ from hPSC was performed by the method we reported previously¹³. Briefly, hPSCs colonies were cultured in mTESR medium until they reached a size of approximately 2 mm, and mesoderm specification was performed by HDM medium (APEL2

(STEMCELL™ technologies), 1x Insulin-Transferrin-Selenium-X (Thermo Fisher Scientific Inc., Waltham, MA) supplemented with 100 ng/ml BMP4 (R&D Systems) for 48 h (D0-2). Subsequently, the concentration of BMP4 was reduced to 10 ng/ml, and the cells were incubated for an additional two days (D2-4). To induction of hematopoietic stem and progenitor cells, the medium was replaced with HDM medium containing 40 ng/ml VEGF (R&D Systems) and 50 ng/ml SCF (R&D Systems) for 2 days (D4-6), and then further differentiated in the HDM medium supplemented with 10 ng/ml TPO (R&D Systems), 50 ng/ml IL-3 (PeproTech, Cranbury, NJ), 50 ng/ml IL-6 (PeproTech), 50 ng/ml Flt-3L (R&D Systems) and 50 ng/ml SCF for 10 days. On day 15, floating cells were harvested and transferred into a 6-well plate and culture with RPMI 1640 (ThermoFisher Scientific, Gibco) media supplemented with FBS and 100 ng/ml M-CSF (PeproTech) for macrophage differentiation. The iMφ were scalable for up to 2 months, with sub-culturing every 7–10 days.

Generation iAlvAssemb by co-culturing of iAEO and iMφ

iAEO was dissociated into a large clump by a few pipetting with 200 µl tips, and parts of iAEO were dissociated with single cells to count cells. To co-culture, 3×10^5 of iAEO and 0.5×10^5 of iMφ were mixed with 500 µl of 50% GFR-matrigels and made a 20 µl matrigel dome. The co-culture medium was used RPMI1640 medium supplemented with 10% FBS, 100 ng/ml MCSF, 2.5 µM SB431542, and 2.5 ng/ml hrFGF7. Y27632 was exclusively added on the first day of culturing, and the co-cultures were typically incubated for one week before further analysis. For enhanced AEC integrity, particularly in AT2 cells with higher expression of SFTPC, low-dose dexamethasone (<5 nM) could be optionally included.

To induce damages in iAlvAssemb, Bleomycin (TCI, Tokyo, Japan) was applied at a concentration of 40 µg/ml for 48 h. Additionally, LPS (Sigma-Aldrich) was treated at a concentration of 1 ng/ml for 24 h. To evaluate the effectiveness of the paracrine factors, GM-CSF (R&D Systems), G-CSF (R&D Systems), and an anti-human GM-CSF monoclonal antibody (Mabtech, Nacka Strand, Sweden) were administered to iMφ. In the case of IL-1β (R&D Systems), and IL-6 (R&D Systems), they were treated in iAEOs using co-culture media.

Live staining with fluorescence dye

To perform live staining of the iAEO, the organoids were treated with LysoTracker Red DND-99 (ThermoFisher Scientific, Invitrogen), which was diluted at a ratio of 1:20000, for a duration of 2 h. For tracking iMφ in the iAlvAssemb, the iMφ cells were labeled using the PKH67 Green Fluorescent Cell Linker Mini Kit for General Cell Membrane Labeling (Sigma-Aldrich), following the instructions provided by the manufacturer. Live cell imaging was carried out using either a fluorescence microscope from Olympus (Tokyo, Japan) or a confocal microscope from Carl Zeiss AG (Oberkochen, Germany).

Real Time-Polymerase Chain Reaction (RT-PCR)

Total RNA was extracted by Easyblue™ Total RNA Extraction Kit (iNtRON Biotechnology, Seongnam-si, Korea) following the manufacturer's instructions. cDNA was synthesized from 1.2 µg of total RNA using SuperScript™ IV First-Strand Synthesis System (Thermo Fisher Scientific). Quantitative RT-PCR was performed using a 1/10 concentration of synthetic cDNA with Fast SYBR Green Master Mix (Applied Biosystems, Waltham, MA) on an 7500 Fast Real-Time PCR instrument system (Applied Biosystems). Gene expression levels were normalized to hGAPDH or hTBP. The primer sequences employed in the study are presented in Supplementary Data 1.

Immunocytochemistry (ICC)

Organoids in the matrigel dome were fixed in 4% PFA (Biosesang, Yongin-si, Korea) for 2–3 min, followed by three washes with dPBS. Subsequently, the samples were treated with 30% sucrose overnight.

Then, samples were embedded in Tissue-Tek® O.C.T. Compound (Sakura Finetek USA, Torrance, CA) and rapidly frozen using liquid nitrogen. Then, 10 µm sections were cut and affixed onto slide glass (MATSUNAMI, Japan).

For immunostaining, cryosections were re-fixed in 4% PFA for 10 min, followed by washing with dPBS. Next, the samples were permeabilized using 0.1% Triton X-100 for 30 min and washed three times with dPBS. To block non-specific binding, the washed samples were treated with 3% BSA. Primary antibodies were diluted in 1% BSA and incubated with the samples overnight at 4 °C. Following fluorescence-conjugated antibodies were utilized: Anti-TTF1 antibody (NKX2-1) (Abcam, Cambridge, UK), Anti-Mature SP-B (SevenHills bioreagents, Cincinnati, OH), Anti-Mature SP-C (SevenHills bioreagents), Anti-HOP (E1) (Santa Cruz Biotechnology, Dallas, TX), Anti-MUC1 (Santa Cruz Biotechnology), Anti-MAC387 (Abcam), Anti-MARCO (Abcam), and Anti-CD204 (MSR1, Abcam). Subsequently, the samples were washed with 0.02% TBST and incubated with secondary antibodies (Jackson Laboratory, Bar Harbor, ME) and Hoechst (Thermo Fisher Scientific) for 1 h at room temperature. After three additional washes in 0.02% TBST, the samples were mounted on slides using Fluorescence Mounting Medium (Dako, Carpinteria, CA) and covered with a cover glass. Finally, fluorescence samples were visualized using confocal microscopy.

ELISA

IL-6, IL1β, and GM-CSF secreted from cells were analyzed using the Quantikine ELISA Kit (R&D system, MN, United States) according to the manufacturer's instructions. Briefly, we collected the culture medium and added it to the microplate strip well with control medium. We then covered the strip and incubate it at room temperature for 1–2 h. After four washes, we added conjugates of IL-6, IL1β, and GM-CSF each and incubated at room temperature for 2 h with cover. After another wash, we added substrate solution and incubated the microplate at room temperature for 20 min in dim light, after which we added stop solution and analyzed the results using a microplate reader at 450 nm.

Cytokine array

Cytokines were analyzed using the Proteome Profiler Human Cytokine Array kit (R&D system, MN, United States). While blocking the membrane, the collected cell culture medium is mixed with array buffer and human cytokine array detection antibody cocktail and incubated for one hour at room temperature. Add sample mixture to membrane and incubate at 4 °C overnight with shaking. After washing, add streptavidin-HRP solution and incubate at room temperature for 30 min with shaking. After another washing, add chemi reagent mix to the membrane and incubate at room temperature for one minute. Remove remaining reagent mix and analyze with autoradiography cassette.

Gene editing

To produce gene-edited cell lines, we designed six guide RNA target sequences per gene and verified their editing efficiency by transfection into 293 T cells. Two guide RNAs with high efficiency were selected and used to produce knockout (KO) lines for CSF2^{-/-} iAEO and IL6^{-/-} IL1b^{-/-} hESC. The target sequences of sgRNA were presented in Supplementary Data 1.

For generating knock-out iAEOs and hESC, the iAEOs and hESC were dissociated into single cells using Accutase. Total 10 µg of plasmids encoding dual guide RNA, CRISPR/Cas9-RFP, and p53DD were then transiently introduced into the 1×10^6 cells by Neon electroporation system (Thermo Fisher scientific). The cell type-specific parameters for electroporation were as follows: hESCs: 1350vols, 20 ms width, 1 pulse, iAEOs: 1400 volts, 30 ms width, 1 pulse. 24 h later, RFP-positive cells were sorted and seeded at low density for clonal selection, followed by genotyping to select knock-out lines.

Exosome isolation

Exosomes were isolated by ExoQuick-TC™ Exosome Precipitation Solution (System Biosciences, CA, United States) following the manufacturer's instructions. Briefly, we collected the culture medium and centrifuged it for 15 min at 3000 g. We then transferred the supernatant to a clean tube and added 1/5 of the volume of ExoQuick-TC. After incubating the well-mixed solution for 12 h at 4 °C, we centrifuged for 30 min at 1500 g, aspirated the supernatant and extracted total RNA from the pellet.

Flow cytometry analysis

Macrophages were collected and incubated with fluorescence-conjugated antibodies for 30 min at 37 °C or 2 h at room temperature. Following fluorescence-conjugated antibodies were utilized: BB700 anti-human CD16 Antibody (BD biosciences), CD45 monoclonal Antibody (2D1) conjugated to APC (eBioscience™, San Diego, CA.), BB515 Mouse Anti-Human CD45 (BD biosciences), Pharmingen™ PE Mouse Anti-Human CD14 (BD biosciences), APC anti-human CD11c antibody (BioLegend, Cat #: 301614) and Pharmingen™ FITC Mouse Anti-Human CD163 (BD biosciences). The stained cells were detected using a BD FACSVerse™ flow cytometer (BD Biosciences), and the data were analyzed using FlowJo_v10 software (FlowJo, LLC, Ashland, OR). To analyze apoptosis and necrosis, we mixed 1000,000 cells each with 1 ul of CellEvent Caspase-3/7 Green Detection Reagent (Thermo, #C10427). Following gentle vortexing, samples were incubated for 60 min at RT, shielded from light. As a final step, 1 ul of a 1 mM solution of SYTOX AADvanced dead cell stain was added. Subsequently, the cells were subjected to analysis using a flow cytometer (CytoFLEX LX, Beckman Coulter), and the data were analyzed using FlowJo_v10 software (FlowJo, LLC, Ashland, OR).

Hematoxylin and Eosin (H&E) staining

The samples on the slide were dehydrated sequentially using 70% and 50% ethanol for 2 min each. Following dehydration, the samples were stained with hematoxylin solution (Sigma-Aldrich) for 7 min. They were then washed in tap water until the water became colorless, which took approximately 15 min. In the subsequent step, the samples were stained with Eosin (Sigma-Aldrich) for 1 min. They were then sequentially dipped in 50%, 70%, 80%, 90%, and 95% ethanol solutions. Subsequently, the samples were incubated with 100% ethanol three times, with each incubation lasting for 2 min. Finally, the samples were mounted using a mounting solution (Thermo Fisher Scientific). The images were visualized using a BX53 microscope from Olympus.

Phagocytosis assay

To compare the phagocytosis ability of iMφ or Alv-iMφ cells isolated from iAlvAssemb, the EZCell™ Phagocytosis Assay Kit (Red E.coli) from BioVision Inc. (Waltham, MA) was utilized. Human AM as an experimental control were purchased from ACEGEN (Fairfield, New Jersey). On the 7th day of co-culture, the Matrigel dome was scraped off with a tip from the culture dish and then gently pipetted to separate the Matrigel from the iAlvAssemb. After centrifugation, the Matrigel layer was removed from the cell pellet and fresh medium was added. Following gentle pipetting to separate the iAEOs and adherent macrophages, the mixture was passed through a 70 μm cell strainer. Through this process, we successfully separated the Alv-iMφ from the iAlvAssemb, as the larger iAEOs remained on the cell strainer, while most of the Alv-iMφ and some dissociated iAEOs passed through with the medium. The isolated ctrl-iMφ and Alv-iMφ were then incubated with a diluted Red E.coli slurry in complete media for 2 h. After incubation, the samples were washed three times with Phagocytosis Assay Buffer. The fluorescent signals were observed using confocal microscopy. The fluorescence intensity per cell was quantified by the Image J software.

Lipid uptake

iMφ or Alv-iMφ cells isolated from iAlvAssemb were treated with 5 μM BODIPY™ 500/510 (Thermo Fisher Scientific, Invitrogen) for 30 min. Subsequently, the cells were washed multiple times with media to remove any unbound dye. The absorbed fluorescent fatty acid analog was then visualized using confocal microscopy. The fluorescence of the cells was quantified using the Image J software.

Live-dead assay and live staining of lipid peroxidation

iAEO, iMφ, and iAlvAssemb cells were cultured in confocal dishes, and after 5 days, they were treated with 40 ng/ml of bleomycin in the media for 48 h to induce cellular damages. For the live-dead assay, the Cyto3D Live-Dead Assay kit from TheWell Bioscience (North Brunswick, NJ) was used. The Cyto3D reagent in the kit was added to the dishes at a ratio of 1:50 of the total volume, and the organoids were incubated at 37 °C for 10 min. Subsequently, the cells were washed multiple times with medium.

To visualize lipid peroxidation in live cells, BODIPY™ 581/591 C11 (Lipid peroxidation sensor) from Thermo Fisher Scientific, Invitrogen was added to the media at a final concentration of 2 μM and incubated for 30 min. Following the incubation, the cells were washed multiple times with the used media. The fluorescent signals were then observed using confocal microscopy.

Transmission electron microscopy

Organoid Matrigel domes were fixed in a solution of 2% glutaraldehyde and 2% paraformaldehyde in DPBS (pH 7.4) for 24 h at 4 °C. After washing, the samples were postfixed in 1% osmium tetroxide (Electron Microscopy Sciences, Hatfield, PA) for 1 h at 4 °C. Dehydration was performed using graded ethanol and propylene oxide, followed by infiltration with propylene oxide and EMBed 812 resin mixtures. The samples were embedded in pure EMBed 812 resin (EMS) and polymerized at 60 °C for 24 h. Ultrathin sections (70 nm) were prepared using an ultramicrotome (Leica, Wetzlar, Germany), stained with uranyl acetate and lead citrate, and examined using a transmission electron microscope (FEI, Tecnai G2 spirit TWIN, Thermo Fisher Scientific). The work was conducted at the EM & Histology Core Facility at the BioMedical Research Center, KAIST.

Single-cell RNA sequencing

For the iAEOs, iAlvAssemb, and LPS-exposed iAlvAssemb assay groups, two biological replicates were collected, and single-cell RNA sequencing (scRNA-seq) was conducted by NICEM research facilities in Seoul National University (Seoul, Korea). Additionally, scRNA-seq was performed on control macrophages, and their sequencing data were analyzed by merging with our previously published GSE133935 data²⁶. To explore gene expression at the single-cell level in human lung tissue, the scRNA-seq data generated by K.J. Travaglini et al.²⁷ were analyzed and visualized using the web-based cellxgene analyzer. The URL provided allows access to this resource: https://cellxgene.cziscience.com/d/krasnow_lab_human_lung_cell_atlas_10x-1.cxg/. The scRNA-seq procedure took place in the same room as we reported in a previous publication²⁶. Briefly, the organoids were disaggregated into individual cells using the Neural Tissue Dissociation Kit (Miltenyi Biotec, NRW, Germany). The cells were washed with a solution containing 0.04% BSA three times. The viability of the cells was assessed using the Countess™ II system (Thermo Fisher Scientific). For library construction, the 10X Chromium Single Cell 3' Reagent Kit v3.1 (10X Genomics, Pleasanton, CA) was employed. The resulting libraries were sequenced on the Illumina NovaSeq 6000 platform (Illumina, San Diego, CA), and the initial sequencing data were converted into FASTQ files using 10x Cell Ranger software (10X Genomics, CA). To process the data, we followed the standard sequencing protocol provided by 10x Genomics, which involved trimming the barcode and unique molecular identifier (UMI) sequence to 26 bp and the mRNA sequence to 98 bp. Subsequently,

the FASTQ files were aligned to the human reference genome (GRCh38). We utilized 10x Cell Ranger software for preliminary data analysis, which generated a file containing a barcode table, a gene table, and a gene expression matrix. Seurat objects were created by using Seurat v5 and were normalized by using normalizing SCTransform, which followed by integration using Harmony³⁰ (Korsunsky, 2019 #33). Integrated object was converted into cloupe file by using loupeR package (<https://github.com/10XGenomics/loupeR>). We utilized Loupe Cell Browser 8.0 (10x Genomics) to perform quality control, analysis, and exploration of the single-cell RNA-seq data.

Bulk RNA sequencing

To perform a comprehensive gene expression analysis of Ctrl-iMφ and Alv-iMφ, Bulk RNA sequencing was carried out by Macrogen (Seoul, Korea). Four groups of samples were prepared, including Ctrl-iMφ, Alv-iMφ isolated from iAlvAssemb (7 days), PBMC-derived monocytes (day 0), and monocyte-derived macrophages (day 7). Libraries were prepared using the TruSeq Stranded mRNA LT Sample Prep Kit (Illumina, San Diego, CA) and sequenced on an Illumina platform. The sequencing data underwent trimming and mapping to the human reference genome (GRCh38) using HISAT2. Transcript assembly was performed using StringTie. The expression levels of each transcript were normalized using fragments per kilobase of transcript per million reads mapped (FPKM). The entire dataset was log2-transformed (FPKM + 1) for further normalization.

For GSEA analysis, Ctrl-iMφ (60-day) and Alv-iMφ from iAlvAssemb (7-day) samples were used. GSEA Desktop v4.1.0 with C8: cell type signature gene sets from Human MSigDB Collections was employed. To compare with AM in human tissue, only peripheral blood-derived monocyte (HPCM) and Human BAL-derived AM (HBAM) data were extracted from a published dataset (GSE174659) by Czarnewski P et al.²⁸. A total of 7080 genes with a *p*-value < 0.05 in HPCM and HBAM were selected, and the fold-change (FC) value of expression in monocytes versus macrophages was calculated. The correlation of iMφ, Alv-iMφ, and monocyte-derived Mφ with tissue-resident AM was independently determined by calculating the Pearson correlation coefficient (*r*) using Prism software (GraphPad Software, San Diego, CA). Sample distance analysis was performed using the Multi Experiment Viewer software (MeV version 4.9.0; <http://mev.tm4.org/>). Differentially expressed genes were sorted based on a fold-change of gene expression (>1.5), and a heatmap was generated using MeV to visualize genes that were upregulated in both Alv-iMφ/mono and HBAM/HPCM. Pathway enrichment analysis using the Reactome Database (<https://reactome.org/>) was conducted in Cytoscape software (www.cytoscape.org). Representative enriched pathway were listed in supplementay Fig. 2B.

To examine the expression changes of AM-enriched genes in Alv-iMφ, we utilized bulk RNA-seq data from a study by Y. Labin et al.¹⁹. This dataset provided a comparison of gene expression across various tissue macrophages in mice. Using relative expression analysis, we identified 480 genes that were enriched in mouse AMs. Subsequently, we investigated the expression changes of the human orthologues of these genes in Alv-iMφ compare to ctrl-iMφ.

Immuno-metabolism analysis

To perform immuno-metabolism analysis using RNA sequencing data, we cultured iMφ with and without GM-CSF (10 ng/ml) for 7 days. The cells were then infected with M.tb (H37Rv) at MOIs of 5 and 10 for 48 h. Following infection, RNA sequencing libraries were prepared, and raw data were processed using the STAR 2.7.11b aligner²⁹, followed by gene expression quantification with RSEM³. We employed the METAF flux pipeline for metabolic flux analysis. Briefly, the metabolic reaction activity score (MRAS) for input data was calculated and metabolic models were constructed. Then flux balance analysis (FBA) was applied to optimize metabolic fluxes. Finally, the results were visualized using

integrated plotting functions. For detailed steps, we referred to the METAF flux tutorial³⁰.

Statistics & reproducibility

Replication details are provided in the figure legends, with each experiment independently repeated at least twice. In experiments on iMφ tissue adaptation, we noted that when iMφ maturity was high before co-culture, the increase in tissue adaptation-related gene expression was either minimal or not observable. consequently, this data was excluded, and only iMφ cells within two month post-differentiation were used in our study

Sample size were indicated in Figure legends and the results are presented as the mean ± standard deviation (SD). The statistical significance of the data was determined using a two-tailed Student's *t*-test or one-way ANOVA with Dunnett's multiple comparisons test, performed by GraphPad Prism 9. *P*-values lower than 0.05 are plotted in the graph.

Graphical Schematics

The graphical schematics illustrating the research methods were created by the author using PowerPoint software. All items were designed as vector-based graphics and were drawn manually without using external sources.

Reporting summary

Further information on research design is available in the Nature Portfolio Reporting Summary linked to this article.

Data availability

The data generated in this study have been deposited in the NCBI's Gene Expression Omnibus (GEO) database under accession code as follows. [GSE231468](#). [GSE269733](#). Additionally, the accession codes for the previously published data used in this study's analysis are provided below. [GSE133935](#). [GSE174659](#). [GSE63340](#). Source data are provided with this paper.

References

- Zepp, J. A. & Morrissey, E. E. Cellular crosstalk in the development and regeneration of the respiratory system. *Nat. Rev. Mol. Cell Biol.* **20**, 551–566 (2019).
- Bissonnette, E. Y., Lauzon-Joset, J. F., Debley, J. S. & Ziegler, S. F. Cross-talk between alveolar macrophages and lung epithelial cells is essential to maintain lung homeostasis. *Front Immunol.* **11**, 583042 (2020).
- Bain, C. C. & MacDonald, A. S. The impact of the lung environment on macrophage development, activation and function: diversity in the face of adversity. *Mucosal Immunol.* **15**, 223–234 (2022).
- Guillot, L. et al. Alveolar epithelial cells: master regulators of lung homeostasis. *Int J. Biochem Cell Biol.* **45**, 2568–2573 (2013).
- Allard, B., Panariti, A. & Martin, J. G. Alveolar macrophages in the resolution of inflammation, tissue repair, and tolerance to infection. *Front Immunol.* **9**, 1777 (2018).
- Manicone, A. M. Role of the pulmonary epithelium and inflammatory signals in acute lung injury. *Expert Rev. Clin. Immunol.* **5**, 63–75 (2009).
- Tao, H., Xu, Y. & Zhang, S. The role of macrophages and alveolar epithelial cells in the development of ARDS. *Inflammation* **46**, 47–55 (2023).
- Doncheva, N. T. et al. Human pathways in animal models: possibilities and limitations. *Nucleic Acids Res* **49**, 1859–1871 (2021).
- Doryab, A. & Groll, J. Biomimetic in vitro lung models: current challenges and future perspective. *Adv. Mater.* **35**, e2210519 (2023).
- Jacob, A. et al. Differentiation of human pluripotent stem cells into functional lung alveolar epithelial cells. *Cell Stem Cell* **21**, 472–488 e410 (2017).

11. Yamamoto, Y. et al. Long-term expansion of alveolar stem cells derived from human iPSCs in organoids. *Nat. Methods* **14**, 1097–1106 (2017).
12. Takata, K. et al. Induced-pluripotent-stem-cell-derived primitive macrophages provide a platform for modeling tissue-resident macrophage differentiation and function. *Immunity* **47**, 183–198 e186 (2017).
13. Han, H. W. et al. Drug discovery platform targeting m. tuberculosis with human embryonic stem cell-derived macrophages. *Stem Cell Rep.* **13**, 980–991 (2019).
14. Seo, H. R. et al. Human pluripotent stem cell-derived alveolar organoid with macrophages. *Int. J. Mol. Sci.* **23**, 9211 (2022).
15. Hofmann, F., Blasche, R., Kasper, M. & Barth, K. A co-culture system with an organotypic lung slice and an immortal alveolar macrophage cell line to quantify silica-induced inflammation. *PLoS One* **10**, e0117056 (2015).
16. Tan, S. Y. & Krasnow, M. A. Developmental origin of lung macrophage diversity. *Development* **143**, 1318–1327 (2016).
17. Rougerie, P., Miskolci, V. & Cox, D. Generation of membrane structures during phagocytosis and chemotaxis of macrophages: role and regulation of the actin cytoskeleton. *Immunol. Rev.* **256**, 222–239 (2013).
18. Dong, Y. et al. CD44 loss disrupts lung lipid surfactant homeostasis and exacerbates oxidized lipid-induced lung inflammation. *Front Immunol.* **11**, 29 (2020).
19. Lavin, Y. et al. Tissue-resident macrophage enhancer landscapes are shaped by the local microenvironment. *Cell* **159**, 1312–1326 (2014).
20. Amit, I., Winter, D. R. & Jung, S. The role of the local environment and epigenetics in shaping macrophage identity and their effect on tissue homeostasis. *Nat. Immunol.* **17**, 18–25 (2016).
21. Shibata, Y. et al. GM-CSF regulates alveolar macrophage differentiation and innate immunity in the lung through PU.1. *Immunity* **15**, 557–567 (2001).
22. Guillemins, M. et al. Alveolar macrophages develop from fetal monocytes that differentiate into long-lived cells in the first week of life via GM-CSF. *J. Exp. Med.* **210**, 1977–1992 (2013).
23. Wright, J. R. Immunoregulatory functions of surfactant proteins. *Nat. Rev. Immunol.* **5**, 58–68 (2005).
24. Chroneos, Z. C., Sever-Chroneos, Z. & Shepherd, V. L. Pulmonary surfactant: an immunological perspective. *Cell Physiol. Biochem* **25**, 13–26 (2010).
25. Chen, Y. W. et al. A three-dimensional model of human lung development and disease from pluripotent stem cells. *Nat. Cell Biol.* **19**, 542–549 (2017).
26. Lee, M. O. et al. Development of a quantitative prediction algorithm for target organ-specific similarity of human pluripotent stem cell-derived organoids and cells. *Nat. Commun.* **12**, 4492 (2021).
27. Travaglini, K. J. et al. A molecular cell atlas of the human lung from single-cell RNA sequencing. *Nature* **587**, 619–625 (2020).
28. Lepzien, R. et al. Monocytes in sarcoidosis are potent tumour necrosis factor producers and predict disease outcome. *Eur. Respir. J.* **58**, 2003468 (2021).
29. Dobin, A. et al. STAR: ultrafast universal RNA-seq aligner. *Bioinformatics* **29**, 15–21 (2013).
30. Huang, Y. et al. Characterizing cancer metabolism from bulk and single-cell RNA-seq data using METAFlex. *Nat. Commun.* **14**, 4883 (2023).

Acknowledgements

This research was supported by grants from the National Research Foundation of Korea (2022M3A9J1072296, RS-2023-00225239,

2021R1C1C1006725, RS-2024-00458236) funded by the Ministry of Science, ICT and Future Planning, Korea Centers for Disease Control and Prevention (2020ER610100, 2023-NS-001-00) and the Korea Research Institute of Bioscience and Biotechnology (KRIBB) Research Initiative Program (KGM4722533, KGM5362521). The funders had no role in the study design, data collection or analysis, decision to publish, or preparation of the manuscript. The authors acknowledge the facilities, and the scientific and technical assistance of the EM & Histology Core Facility and Dr. Yongsuk Hur at the BioMedical Research Center, Korea Advanced Institute of Science and Technology. Additionally, ChatGP-T (OpenAI, San Francisco, CA, USA) assisted with sentence editing.

Author contributions

All authors have read and approved the published version of the manuscript. Conceptualization: J.-H.K. and M.-O.L., Validation: J.S.K., Y.L., M.J.K., J.M.L., and M.-O.L., Formal analysis: J.S.K., Y.L., D.G., K.-C.Ko, and M.-O.L., Bioinformatics analysis: D.G. and M.-O.L., M. tuberculosis infection and analysis: V.D. and C.W., Manuscript writing and review: J.S.K., Y.L., J.-H.K., and M.-O.L.

Competing interests

The authors declare no competing interests.

Additional information

Supplementary information The online version contains supplementary material available at <https://doi.org/10.1038/s41467-025-58450-w>.

Correspondence and requests for materials should be addressed to Jung-Hyun Kim or Mi-Ok Lee.

Peer review information *Nature Communications* thanks Maziar Divan-gahi, and the other, anonymous, reviewer(s) for their contribution to the peer review of this work. A peer review file is available.

Reprints and permissions information is available at <http://www.nature.com/reprints>

Publisher's note Springer Nature remains neutral with regard to jurisdictional claims in published maps and institutional affiliations.

Open Access This article is licensed under a Creative Commons Attribution-NonCommercial-NoDerivatives 4.0 International License, which permits any non-commercial use, sharing, distribution and reproduction in any medium or format, as long as you give appropriate credit to the original author(s) and the source, provide a link to the Creative Commons licence, and indicate if you modified the licensed material. You do not have permission under this licence to share adapted material derived from this article or parts of it. The images or other third party material in this article are included in the article's Creative Commons licence, unless indicated otherwise in a credit line to the material. If material is not included in the article's Creative Commons licence and your intended use is not permitted by statutory regulation or exceeds the permitted use, you will need to obtain permission directly from the copyright holder. To view a copy of this licence, visit <http://creativecommons.org/licenses/by-nc-nd/4.0/>.

© The Author(s) 2025